nature communications

Article

https://doi.org/10.1038/s41467-025-59376-z

Suppressing CO_x in oxidative dehydrogenation of propane with dual-atom catalysts

Received: 5 November 2024

Accepted: 16 April 2025

Published online: 19 May 2025

Check for updates

Yongbin Yao[1,2,11], Jingnan Wang[3,11], Fei Lu[4,11], Wenlin Li[5,11], Bingbao Mei[6,11], Lifeng Zhang[3], Wensheng Yan[7], Fangli Yuan[8], Guiyuan Jiang[9], Sanjaya D. Senanayake[10] ✉ & Xi Wang[1,2] ✉

Oxidative dehydrogenation of propane (ODHP) is a promising route for propylene production, but achieving high selectivity towards propylene while minimizing CO_x byproducts remains a significant challenge for conventional metal oxide catalysts. Here we propose a solution to this challenge by employing atomically dispersed dual-atom catalysts ($M_1M'_1$-TiO_2 DACs). Ni_1Fe_1-TiO_2 DACs exhibit an ultralow CO_x selectivity of 5.2% at a high propane conversion of 46.1% and 520 °C, with stable performance for over 1000 hours. Mechanistic investigations reveal that these catalysts operate via a cooperative Langmuir-Hinshelwood mechanism, distinct from the Mars-van Krevelen mechanism typical of metal oxides. This cooperative pathway facilitates efficient conversion of propane and oxygen into propylene at the dual-atom interface. The superior selectivity arises from facile olefin desorption from the dual-atom sites and suppressed formation of electrophilic oxygen species, which are preferentially adsorbed on Fe_1 sites rather than oxygen vacancies. This work highlights the potential of dual-atom catalysts for highly selective ODHP and provides insights into their unique catalytic mechanism.

The rising demand for propylene, driven by its widespread use in the production of polymers and chemicals, has intensified research into efficient and sustainable production methods[1,2]. Oxidative dehydrogenation of propane (ODHP) offers a promising alternative to conventional propane dehydrogenation (PDH)[3,4], as it is exothermic and less susceptible to coke formation. However, achieving high selectivity towards propylene remains a major challenge. Conventional metal oxide catalysts (MOCs), typically operating via a Mars-van Krevelen (MvK) mechanism[5–12], suffer from high CO_x selectivity (>25%) at high propane conversions (>25%) due to the formation of electrophilic oxygen species on oxygen vacancies[13,14]. Despite extensive efforts, few MOC-based catalysts have achieved CO_x selectivity below 10% while maintaining high propane conversion.

To address this limitation, we explore the potential of cooperative dual-atom catalysis, where distinct active sites can synergistically activate propane and oxygen. This approach aims to minimize the

[1]Key Laboratory of Luminescence and Optical Information, Ministry of Education, School of Physical Science and Engineering, Beijing Jiaotong University, Beijing 100044, P. R. China. [2]Chemistry and Chemical Engineering Guangdong Laboratory, Shantou 515031, P. R. China. [3]Institute of Molecular Engineering Plus, College of Chemistry, Fuzhou University, Fuzhou 350108, P. R. China. [4]College of Physical Science and Technology, Yangzhou University, Yangzhou 225002, P. R. China. [5]College of Chemistry and Chemical Engineering, State Key Laboratory of Clean and Efficient Coal Utilization, Taiyuan University of Technology, Taiyuan 030024, P. R. China. [6]Shanghai Institute of Applied Physics, Chinese Academy of Sciences, Shanghai 201204, P. R. China. [7]National Synchrotron Radiation Laboratory, University of Science and Technology of China, Hefei, Anhui 230026, P. R. China. [8]State Key Laboratory of Mesoscience and Engineering, Institute of Process Engineering, Chinese Academy of Sciences, Beijing 100190, P. R. China. [9]State Key Laboratory of Heavy Oil Processing, China University of Petroleum, Beijing 102249, P. R. China. [10]Chemistry Division, Brookhaven National Laboratory, Upton, NY 11973, USA. [11]These authors contributed equally: Yongbin Yao, Jingnan Wang, Fei Lu, Wenlin Li, Bingbao Mei. ✉e-mail: ssenanay@bnl.gov; xiwang@bjtu.edu.cn

formation of electrophilic oxygen species by promoting O_2 adsorption on specific metal sites rather than oxygen vacancies. While the concept of cooperative catalysis has been demonstrated in other systems[15–21], its application in heterogeneous ODHP remains largely unexplored.

Herein, we report a series of supported dual-atom catalysts (6 types, $M_1M'_1$-TiO_2 DACs) synthesized via a modified cation-exchange strategy[22–24]. These catalysts, featuring atomically dispersed metal pairs on a TiO_2 support, demonstrate exceptional performance in ODHP. In particular, Ni_1Fe_1-TiO_2 DACs exhibit an ultralow CO_x selectivity of 5.2% at a high propane conversion of 46.1% and 520 °C, with remarkable stability for over 1000 h. This performance surpasses previously reported catalysts, which typically show limited stability beyond 300 h under continuous ODHP conditions.

Results

Catalytic performance

The catalytic performance of metal oxide catalysts (MOCs), M_1-TiO_2 single-atom catalysts (SACs), and $M_1M'_1$-TiO_2 dual-atom catalysts (DACs) was evaluated for oxidative dehydrogenation of propane (ODHP). Our optimization revealed that when the loading of M_1 and M'_1 in $M_1M'_1$-TiO_2 was fixed at ~3 wt %, DACs (e.g. Fe_1Ni_1-TiO_2) exhibited high performance. However, deviations from this optimal metal (e.g. Fe and Ni) loading led to decreased propene selectivity (Supplementary Fig. 1). As shown in Fig. 1a, Fe_1Ni_1-TiO_2 achieved an ultralow CO_x selectivity of 5.2% while maintaining a high propane conversion of 46.1% at 520 °C. This performance surpasses previously reported metal-oxide-based ODHP catalysts (Supplementary Table 1), where CO_x selectivity typically exceeds 10% at comparable propane conversions (>25%). In contrast, both SACs and MOCs generated higher levels of CO_x under identical conditions. Fe_1Ni_1-TiO_2 also exhibited excellent olefin selectivity (90.6%) across a wide temperature range (420–520 °C, Supplementary Fig. 2). This superior CO_x suppression was consistently observed for other $M_1M'_1$-TiO_2 DACs, demonstrating the inherent advantage of dual-atom structures over single-atom structures or MOCs in ODHP.

Further confirmation of the enhanced activity of DACs was obtained through an assessment of propane reaction rates. With a TOF of 56.2 s^{-1}, the Ni_1Fe_1-TiO_2 catalyst exhibited significantly higher

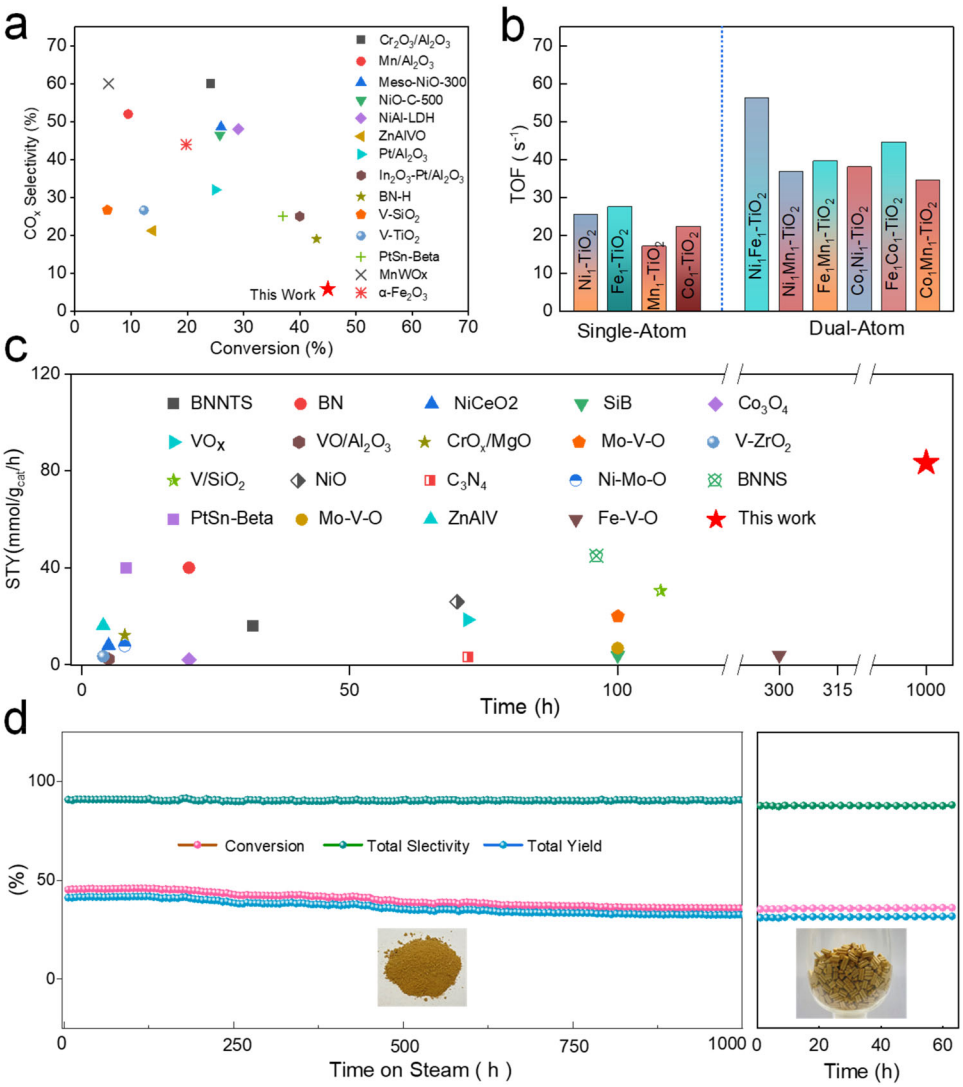

Fig. 1 | Catalytic performance of different catalysts for ODHP. a The CO_x selectivity of as-prepared Ni_1Fe_1-TiO_2 DACs with reported ODHP catalysts (Supplementary Table 1). **b** Comparison of the TOF of C_3H_8 versus time on as-prepared DACs and SACs (Reaction conditions: C_3H_8: O_2: N_2 = 1:1:1, Total flow = 36 mL/min, Catalyst weight = 0.1 g, Temperature = 520 °C). **c** Comparison of STY versus time on our Ni_1Fe_1-TiO_2 DACs with reported ODHP catalysts. The STY, defined as the olefin production rate per gram of catalyst per hour, is presented in Supplementary Table 2 along with all reaction conditions and catalytic results. **d** The durability of Ni_1Fe_1-TiO_2 powder and shaping samples. Reaction conditions: C_3H_8: O_2: N_2 = 1:1:1, Volume rates of C_3H_8 = 12 mL/min with weight hour space velocity (WHSV) = 8.8 h^{-1}, 520 °C.

https://doi.org/10.1038/s41467-025-59376-z

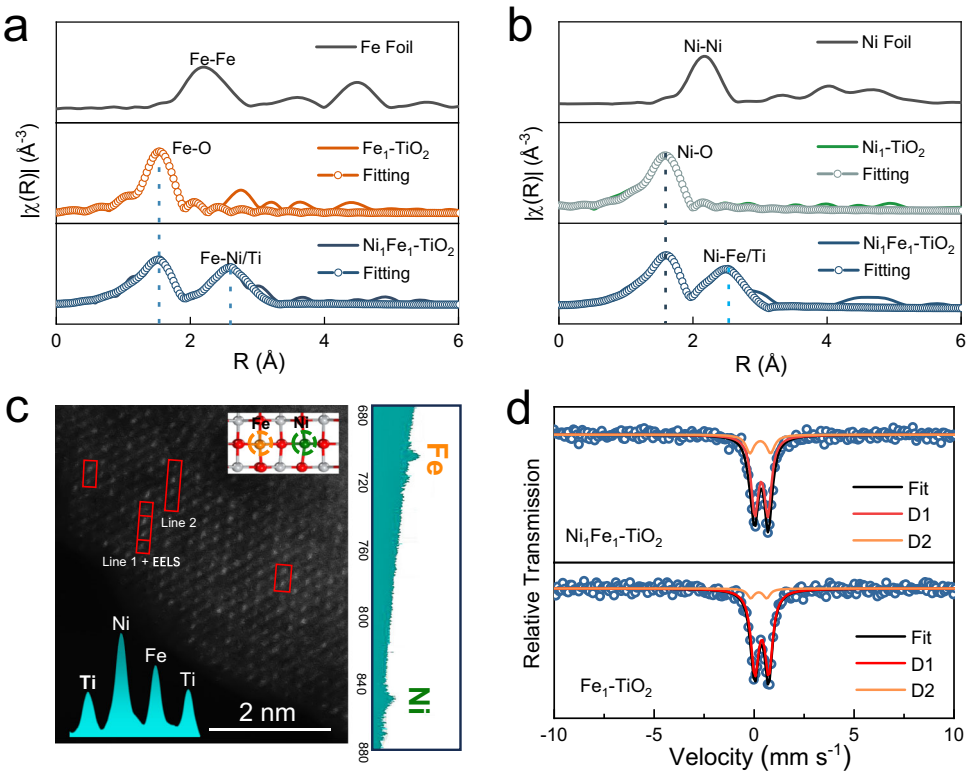

Fig. 2 | Structural characterization of Ni_1Fe_1-TiO_2 DACs. a, **b** k^2-weighted EXAFS spectra of (**a**) Fe *K*-edge and (**b**) Ni *K*-edge for Ni_1Fe_1-TiO_2 and reference samples. *k* denotes the wave vector of the photoelectron. **c** The AC-STEM image, the line intensity profile of line 1 (insert, bottom), and corresponding EELS (side) for Ni_1Fe_1-TiO_2. The top view of Ni_1Fe_1-TiO_2 DACs is shown in the top right corner. **d** Experimental ^{57}Fe Mössbauer spectra of Fe_1-TiO_2 and Fe_1Ni_1-TiO_2 measured at 293 K. The doublets D1 and D2 represent Fe^{3+} and Fe^{2+} states, respectively.

activity compared to the monometallic Ni_1-TiO_2 and Fe_1-TiO_2 catalysts. This translated to an ultrahigh olefin yield of 40.7% at 520 °C, surpassing Fe_1-TiO_2 and Ni_1-TiO_2 by twofold (Supplementary Fig. 3). This enhanced catalytic activity was consistently observed across various DAC and SAC (Supplementary Figs. 4–5), underscoring the benefits of the dual-atom architecture.

The long-term stability and productivity of Ni_1Fe_1-TiO_2 were assessed by evaluating the olefin space-time yield (STY) over 1000 h of continuous operation (Fig. 1c). While previous studies have reported high olefin STY values for catalysts composed of multi-elemental, nonmetal, or alloy materials (e.g., V-Fe-O, BN, PtSn/Beta, Supplementary Table 2), MOC-based ODHP catalysts have generally struggled to achieve STY values exceeding 50 $mmolg_{cat}^{-1}h^{-1}$ after 300 h. Remarkably, Ni_1Fe_1-TiO_2 exhibited an ultrahigh olefin STY of 83.3 $mmolg_{cat}^{-1}h^{-1}$ after 1000 h at 520 °C, effectively overcoming the trade-off between STY and stability. This performance surpasses state-of-the-art catalysts in terms of olefin yield and long-term durability (Fig. 1c, d, Supplementary Table 2). Furthermore, we successfully scaled up production to kilogram-scale quantities while maintaining ease in shaping the catalyst structure, highlighting its potential for industrial applications (Supplementary Fig. 6). The shaped Ni_1Fe_1-TiO_2 catalyst demonstrated comparable performance as its powdered counterpart, and also operated stably with a high olefin selectivity of ~90% at 520 °C (Fig. 1d, right).

Structure and characterization of dual-atom catalysts

The catalysts were synthesized via a solid-state calcination, a robust and sophisticated method involving a mixture of TiO_2, metal oxide (M = Fe_2O_3, CoO, NiO, MnO, MgO,...) salts, and alkali metal carbonates heated to high temperatures (Supplementary Fig. 7). The supported and catalysis were thoroughly characterized. The TiO_2 nanosheet support exhibited a BET surface area of 78.2 m^2/g, with an interlayer spacing calculated to be 0.95 Å (Supplementary Figs. 8–10). Both SACs and DACs, including Ni_1Fe_1-TiO_2, Ni_1-TiO_2, and Fe_1-TiO_2, exhibited a lamellar structure consistent with the BET surface area >100 m^2/g (Supplementary Figs. 11–14, Supplementary Table 3). In Ni_1Fe_1-TiO_2, Ni and Fe atoms were homogeneously dispersed throughout the nanosheets without any discernible agglomeration.

X-ray absorption near-edge structure (XANES) analysis confirmed the dual-atom structure of Ni_1Fe_1-TiO_2. Compared to Ni_1-TiO_2 and Fe_1-TiO_2, Ni_1Fe_1-TiO_2 displayed a dual scattering pathway in the k^2-weighted extended X-ray absorption fine structure (EXAFS) spectra (Fig. 2a, b, Supplementary Fig. 15, Supplementary Table 4), consistent with the two domains observed in the wavelet transform signature (Supplementary Fig. 16). This indicates that the Ti lattice of the TiO_2 nanosheet support effectively confines isolated Ni and Fe atoms in close proximity[25–27]. Pre-edge features in the XANES spectra clearly distinguished the electronic structures of Ni_1Fe_1 dual-atom sites from those of the isolated Ni_1-TiO_2 and Fe_1-TiO_2 sites. Charge transfer within the Ni_1-Fe_1 pair was evident, with Ni in Ni_1Fe_1-TiO_2 displaying a higher valence shift compared to Ni in Ni_1-TiO_2, and Fe in Ni_1Fe_1-TiO_2 exhibiting a lower valence shift compared to Fe in Fe_1-TiO_2. (Supplementary Figs. 17–20).

Aberration-corrected scanning transmission electron microscopy (AC-STEM) and atomic-resolution electron energy loss spectroscopy (EELS) provided direct visualization of the heteronuclear dual-atom structure in Ni_1Fe_1-TiO_2 (Fig. 2c). The distinct line intensity profiles of Ni and Fe signals provide direct evidence for observing Ni_1-Fe_1 pairs along the Ti column (inset in Fig. 2c, Supplementary Fig. 21). The measured distance between Ni_1 and Fe_1 (3.1 Å) aligned with the scattering distance observed in XANES analysis, confirming their substitution for Ti sites and the formation of Ni_1-Fe_1 dual-atom sites within

https://doi.org/10.1038/s41467-025-59376-z

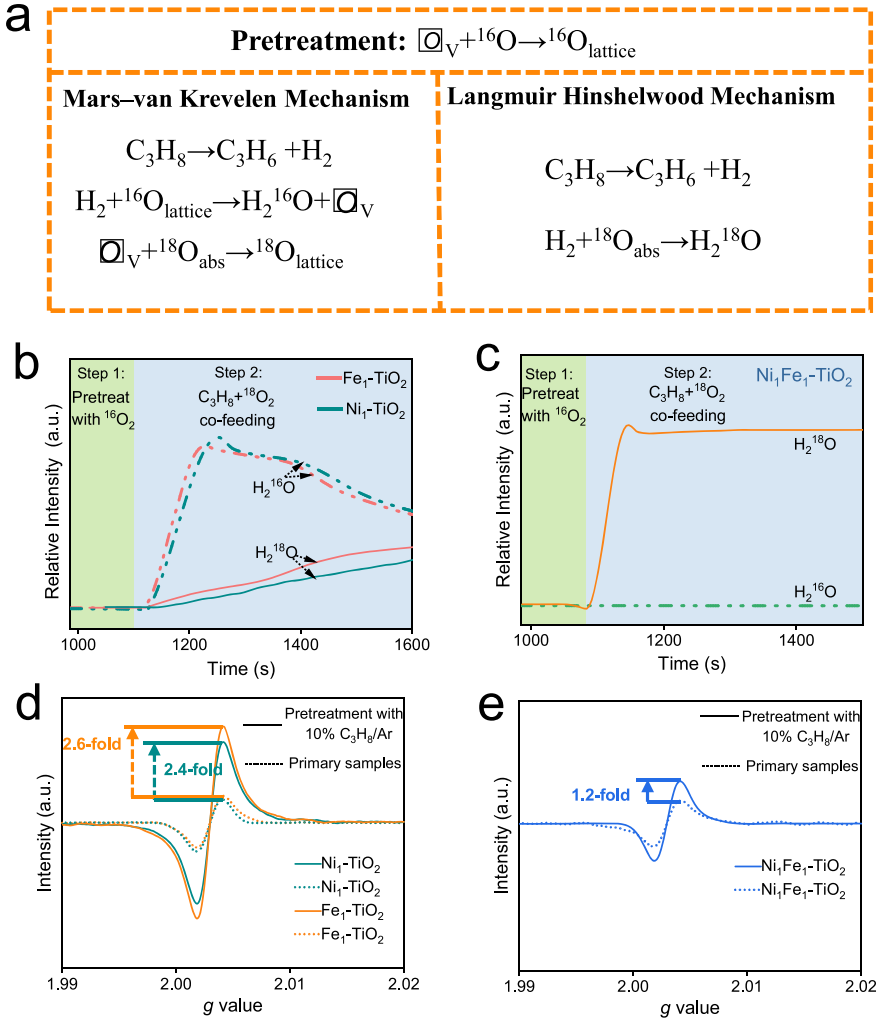

Fig. 3 | Catalysis mechanism studies. a Schematic diagram of MvK and L-H mechanisms. **b**, **c** $H_2{}^{16}O$ and $H_2{}^{18}O$ response signals of reactions of $^{18}O_2$–C_3H_8 mixture on Ni_1-TiO_2, Fe_1-TiO_2, and Ni_1Fe_1-TiO_2 followed by He purge at 520 °C (10% C_3H_8/Ar, 10 mL/min and 10% $O^{18}{}_2$/Ar, 10 mL/min). **d**, **e** EPR spectra of spent Ni_1-TiO_2, Fe_1-TiO_2, and Ni_1Fe_1-TiO_2 catalysts without and with pretreatment with 10% C_3H_8/Ar at 520 °C for 2 h.

the TiO_2 lattice (Supplementary Fig. 22). Notably, when mono-metal oxides (NiO or Fe_2O_3) were introduced during synthesis, Fe and Ni exhibited a preference for isolated FeO_5 (Fe_1-TiO_2) or NiO_5 (Ni_1-TiO_2) configurations. The single-atom structure of Fe_1-TiO_2 and Ni_1-TiO_2 was further confirmed by AC-STEM (Supplementary Fig. 23) and XANES measurements (Fig. 2a, b, Supplementary Fig. 24), which revealed well-defined monodispersed spots along the Ti lattice and distinct features corresponding to Ni(1)/Fe(1)-O(5) coordination in the isolated systems (Supplementary Table 5).

Mössbauer spectrometry was employed to probe the Fe environments in Ni_1Fe_1-TiO_2 and Fe_1-TiO_2. Compared to Fe_1-TiO_2, the proportion of Fe^{2+} species increased from 9.3% to 21.0% in Ni_1Fe_1-TiO_2 (Fig. 2d), indicating a decrease in the average oxidation state of Fe[28–30]. This shift in oxidation states between individual Ni_1 and Fe_1 atoms can be attributed to charge compensation within the Fe-Ni pairs in Ni_1Fe_1-TiO_2. This charge redistribution facilitates pairing between divalent Ni^{2+} and trivalent Fe^{3+} to fulfill local coordination requirements and maintain overall charge neutrality, rather than dimerization involving solely +2/ + 3 charged species[31–33].

The synthetic procedure was extended to create a library of heteronuclear dual-atom catalysts in TiO_2. A series of M_1-TiO_2 catalysts (M = Fe, Co, Ni, Mn) (Supplementary Figs. 25–26, Supplementary Table 4) and $M_1M'_1$-TiO_2 DACs ($M_1M'_1$ = Ni_1Fe_1, Co_1Ni_1, Co_1Mn_1, Ni_1Mn_1, Fe_1Mn_1, Fe_1Co_1) were successfully synthesized using different precursors. Comprehensive structural characterizations, including XRD analysis, TEM imaging, AC-STEM observations, and XANES measurements (Supplementary Figs. 27–34, Supplementary Table 5), confirmed the dual-atom feature in these catalysts.

Catalytic mechanism

In the ODHP process, MOCs undergo either the commonly observed MvK mechanism (Fig. 3a, left) or an alternative Langmuir-Hinshewood (L-H) mechanism (Fig. 3a, right), depending on whether lattice oxygen exchange is involved. To verify the mechanism, we conducted a study using the $^{16}O/^{18}O$ isotope exchange method. Catalysts were initially pre-treated with $^{16}O_2$ to ensure lattice oxygen was predominantly ^{16}O (Fig. 3a). Upon switching to a reaction gas mixture of $^{18}O_2$ and C_3H_8, Ni_1-TiO_2 and Fe_1-TiO_2 exhibited $H_2{}^{16}O$ production, indicative of lattice oxygen involvement (Fig. 3b). This $H_2{}^{16}O$ signal gradually decreased as lattice ^{16}O was replaced by ^{18}O from the gas phase, consistent with the MvK mechanism[14,34]. In contrast, Ni_1Fe_1-TiO_2 showed negligible $H_2{}^{16}O$ production and a rapid $H_2{}^{18}O$ response (Fig. 3c), with no evidence of $^{16}O_2$ or $^{16}O^{18}O$ formation (Supplementary Fig. 35). This suggests that lattice oxygen exchange is minimal, and the ODHP reaction over Ni_1Fe_1-TiO_2 likely proceeds through the L-H mechanism, where C_3H_8 and O_2 co-adsorb on the catalyst surface.

https://doi.org/10.1038/s41467-025-59376-z

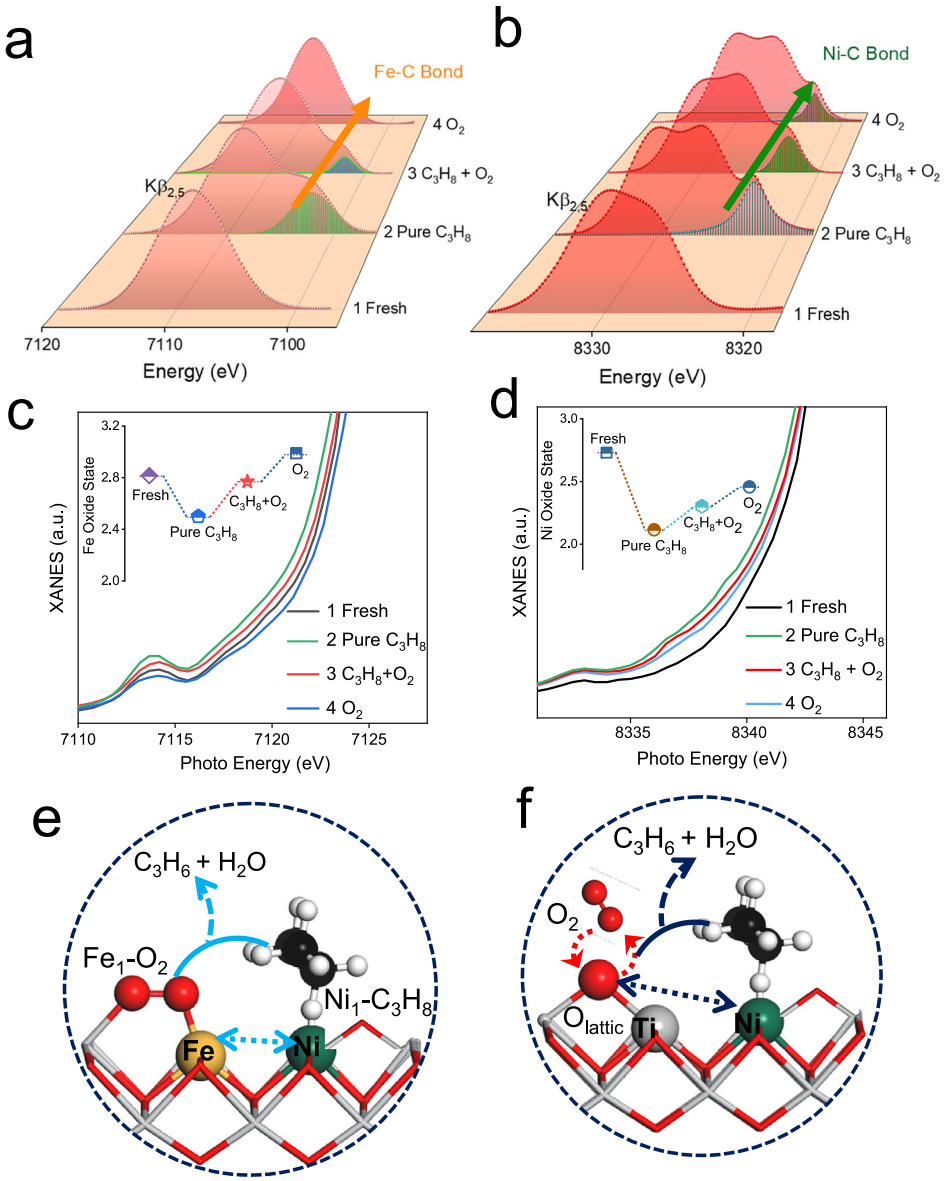

Fig. 4 | The adsorption capabilities of DACs towards C_3H_8 and O_2. **a**, **b** In-situ $K\beta_{2,5}$ and $K\beta''$ mainline XES spectra recorded Ni_1Fe_1-TiO_2 under different steps at 520 °C. **c**, **d** In-situ XANES absorption edge spectra for the Ni K-edge and Fe K-edge of Ni_1Fe_1-TiO_2 under different steps at 520 °C. **e** Schematic illustration of C_3H_8 (Ni site) and O_2 (Fe site) reaction over Ni_1Fe_1-TiO_2. **f** Schematic illustration of C_3H_8 (Ni site) and O_{lattic} reaction over Ni_1-TiO_2. In-situ XES and XANES were measured by gradually increasing the temperature to 520 °C within a helium stream after stabilization; different gases were sequentially introduced (pure C_3H_8 → C_3H_8 + O_2 → pure O_2), and spectra were collected at each stabilized condition.

To further probe the involvement of lattice oxygen, electron paramagnetic resonance (EPR) spectroscopy was employed to quantify oxygen vacancies in spent SACs and DACs before and after pre-treatment with 10% C_3H_8/Ar at 520 °C. The EPR intensity of oxygen vacancies increased approximately twofold for Ni_1-TiO_2 and Fe_1-TiO_2 after C_3H_8 pre-treatment (Fig. 3d, Supplementary Fig. 36), whereas only a 1.2-fold increase was observed for Ni_1Fe_1-TiO_2 (Fig. 3e). The generation of more oxygen vacancies in SACs compared to DACs further supports the notion that SACs experience an MvK pathway while DACs undergo an L − H one for oxygen activation.

Mechanistic insights from in-situ spectroscopy

To investigate the interplay between reactants (C_3H_8, O_2) and the active sites (Fe, Ni) in Ni_1Fe_1-TiO_2, we employed in-situ X-ray emission spectroscopy (XES). This technique is particularly sensitive to the chemical environment of transition metals and can effectively differentiate between ligands with similar atomic numbers, such as C, N, and O[35–37]. We designed an in-situ XES experiment by gradually increasing the temperature to 520 °C within a helium stream and acquiring the 'fresh' spectrum after stabilization. Subsequently, different gases were sequentially introduced (pure C_3H_8 → C_3H_8 + O_2 → pure O_2), and spectra were collected following each stabilized condition.

For Ni_1Fe_1-TiO_2 catalysts, Fig. 4a and b present the $K\beta_{2,5}$ XES of Ni and Fe during distinct steps, respectively. The XES spectra revealed both Ni-C and Fe-C bonds in a pure C_3H_8 atmosphere with binding energies of 7102.1 eV and 8326.1 eV, respectively[38,39]. Upon the addition of O_2, there was a gradual disappearance of Fe-C bonds compared to persistent but weakened Ni-C bonds observed. After removing C_3H_8, Ni-C bonds remained while Fe-C bonds almost completely disappeared indicating that Ni sites exhibit higher propensity for propane adsorption than Fe sites.

This preferential adsorption behavior was further corroborated by temperature-programmed desorption (TPD) experiments. C_3H_8 desorption capacity was lowest at the Fe_1 site in Fe_1-TiO_2 compared to Ni_1-TiO_2 and Ni_1Fe_1-TiO_2 (Supplementary Fig. 37), while a minor O_2 desorption peak at 432.0 °C was observed for Ni_1-TiO_2, which was absent in the other two samples (Supplementary Fig. 38). These results are consistent with the XES data, suggesting preferential adsorption of C_3H_8 on Ni and O_2 on Fe in Ni_1Fe_1-TiO_2.

In-situ XANES analysis provided insights into the valence state evolution of Fe and Ni in Ni_1Fe_1-TiO_2 under the same reaction conditions as the XES experiments. Changes in the Ni K-edge and Fe K-edge XANES spectra (Fig. 4c, d) revealed that: (1) C_3H_8 purging at 520 °C induced a shift to lower energies, indicating reduction of both Ni and Fe; (2) Introducing O_2 significantly increased the Fe valence state with minimal impact on the Ni valence state; (3) Removing C_3H_8 under O_2 flow led to a further increase in the Fe valence state. These findings, supported by DFT calculations (Supplementary Fig. 39), suggest that Fe sites are primarily responsible for oxygen activation. The limited change in the Ni valence state upon O_2 introduction is attributed to the strong adsorption of residual C_3H_8 on Ni sites. Further in-situ XANES studies confirmed the facile reduction of Ni by C_3H_8 (Supplementary Figs. 40–43) and the strong interaction between Fe_1 sites and O_2 (Supplementary Figs. 44–45). Collectively, the in-situ XES, C_3H_8/O_2-TPD, and in-situ XANES data provide compelling evidence for distinct roles of Ni and Fe in Ni_1Fe_1-TiO_2: Ni sites preferentially adsorb C_3H_8, while Fe sites favor O_2 adsorption and activation.

DFT calculations were performed to elucidate the ODHP reaction pathway over Ni_1Fe_1-TiO_2 (Supplementary Figs. 46–47). The results suggest a highly efficient L-H mechanism (Fig. 4e) where C_3H_8 dehydrogenation occurs at Ni_1 sites, while activated O_2 on Fe_1 sites promotes hydrogen coupling to form H_2O and C_3H_6. In contrast, DFT calculations for the single-atom catalysts (Ni_1-TiO_2 and Fe_1-TiO_2) suggest an MvK mechanism (Supplementary Figs. 48–51, Fig. 4f), highlighting the distinct mechanistic behavior of DACs and SACs. The key difference lies in the involvement of lattice oxygen exchange in the MvK mechanism, where oxygen vacancies play a crucial role in driving propane dehydrogenation.

Suppression of CO_x formation

One of the major challenges faced by ODPH catalysts is the generation of significant amounts of valueless CO_x (>30% in selectivity for MOCs). A consensus among literature reports suggests that the majority of CO_x species originate from propylene oxidation reaction with electrophilic oxygen species generate by lattice oxygen exchange through Mv-K pathways (Supplementary Fig. 52)[14,40,41]. To assess the propensity for C_3H_6 over-oxidation, we analyzed C_3H_6-TPD profiles (Fig. 5a). Ni_1Fe_1-TiO_2 exhibited a lower C_3H_6 desorption temperature (138.7 °C) compared to Ni_1-TiO_2 (170.1 °C) and Fe_1-TiO_2 (162.2 °C), indicating weaker C_3H_6 binding and enhanced propylene release. This observation was corroborated by in-situ diffuse reflectance infrared Fourier transform spectroscopy (DRIFTS) analysis, which revealed significantly faster C_3H_6 desorption rates over Ni_1Fe_1-TiO_2 compared to the single-atom counterparts (Supplementary Figs. 53–55). DFT calculations further support this trend, showing lower C_3H_6 desorption energies from the Ni_1 site in Ni_1Fe_1-TiO_2 compared to Ni and Fe sites in Ni_1-TiO_2 and Fe_1-TiO_2 (Supplementary Fig. 56). The facile desorption of C_3H_6 from Ni_1Fe_1-TiO_2 effectively mitigates its over-oxidation.

To identify potential intermediates in the C_3H_6 over-oxidation pathway, we performed in-situ DRIFTS analysis under reaction conditions (Fig. 5b). Ni_1Fe_1-TiO_2 displayed a distinct C = C stretching vibration at 1650 cm^{-1}, characteristic of C_3H_6, whereas Ni_1-TiO_2 and Fe_1-TiO_2 exhibited a prominent peak at 1738 cm^{-1}, indicative of aldehyde groups[42,43]. Furthermore, a distinct CO_2 gas-phase peak at 2349 cm^{-1} was observed for Ni_1-TiO_2 and Fe_1-TiO_2, but was barely discernible for Ni_1Fe_1-TiO_2 (Supplementary Fig. 57). These findings suggest that acrolein, an aldehyde species, is a key intermediate in the deep oxidation of propylene to CO_x. The suppression of acrolein formation over Ni_1Fe_1-TiO_2 effectively limits CO_x generation.

Importantly, this suppression of over-oxidation was observed for all synthesized $M_1M'_1$-TiO_2 DACs (6 types, Supplementary Figs. 58–67), highlighting the general efficacy of this catalyst design. To understand the underlying cause, we examined the nature of oxygen species using electron paramagnetic resonance (EPR) spectroscopy. Fe_1-TiO_2 and Ni_1-TiO_2 exhibited a weak isotropic signal at $g = 2.02$ (Fig. 5c, d), indicative of electrophilic O_2^- species[44,45], which are known to promote CO_x formation. This signal was nearly absent in Ni_1Fe_1-TiO_2, suggesting a lower concentration of electrophilic oxygen species. This is attributed to the preferential adsorption of O_2 on Fe_1 sites in Ni_1Fe_1-TiO_2, rather than on oxygen vacancies as in MOCs, leading to a reduced contribution of electrophilic oxygen.

Figure 5e illustrates the proposed mechanisms of CO_x formation for NiO_x and Ni_1Fe_1 species. Trace amounts of electrophilic oxygen species and relatively low propylene desorption energy for the Ni_1Fe_1-TiO_2 catalyst effectively suppressed acrolein (a significant byproduct in the deep oxidation process) formation, thereby reducing CO_x generation. In contrast, the stronger propylene adsorption on Ni_1 or Fe_1-TiO_2 catalysts facilitated the formation of acrolein from propylene with electrophilic oxygen species, leading to further overoxidation to CO_x.

Discussion

Atomically dispersed dual-atom catalysts (DACs) offer a promising avenue for enhancing ODHP by mitigating CO_x formation. Here, we report a general synthetic strategy for $M_1M'_1$-TiO_2 DACs and demonstrate their exceptional performance in ODHP. Specifically, Ni_1Fe_1-TiO_2 exhibits an ultralow CO_x selectivity of 5.2% while maintaining a high propane conversion of 46.1% for 1000 h at 520 °C. Mechanistic investigations, combining experimental characterization and theoretical calculations, reveal a Langmuir-Hinshelwood mechanism facilitated by synergistic interactions between the Ni_1 and Fe_1 sites. Crucially, the Fe_1 sites promote O_2 adsorption, effectively suppressing the formation of electrophilic oxygen species that lead to CO_x generation. Furthermore, the Ni_1Fe_1-TiO_2 DAC exhibits a lower energy barrier for propylene desorption compared to single-atom Ni_1-TiO_2 and NiO catalysts, contributing to its enhanced catalytic efficiency. This work highlights the potential of precisely engineered DACs to optimize ODHP performance by manipulating the adsorption and activation of both propane and oxygen.

Methods

Materials

Titanium (IV) oxide (TiO_2, rutile, 99.5%, CAS: 1317-80-2) and potassium carbonate (K_2CO_3, 99.9%, CAS: 534–17-8) were purchased from Alfa Aesar. Manganese (II) oxide (MnO, 99.5%), nickel (II) oxide (NiO, 99%), iron(III) oxide (Fe_2O_3, 99.9%), and cobalt(II) oxide (CoO, 99.9%) were obtained from Innochem. Propane (C_3H_8, 99.9%), oxygen (O_2, 99.999%), and nitrogen (N_2, 99.999%) were supplied by Beijing Huatong Jingke Gas Chemical Co., LTD.

Catalyst synthesis

TiO_2 nanosheets. Briefly, K_2CO_3 (1.11 g), rutile TiO_2 (2.77 g), and Li_2CO_3 (0.2 g) were ground for 1 h and calcined at 900 °C for 1.5 h. The resulting product was ground again for 1 h and calcined at 1000 °C for 20 h to yield layered titanate ($K_{0.8}Ti_{1.73}Li_{0.27}O_4$). The titanate was then protonated by treatment with 1 mol L^{-1} HCl (100 mL/g titanate) with daily replacement of the HCl solution for 3 days. The resulting catalysis was washed with distilled water until neutral and dried under vacuum.

M_1-TiO_2 nanosheets. M_1-TiO_2 nanosheets (M = Mn, Fe, Co, Ni) were prepared by adapting a solid reaction method[1]. Stoichiometric quantities of the respective metal oxide (MnO, Fe_2O_3, CoO, or NiO), K_2CO_3,

https://doi.org/10.1038/s41467-025-59376-z

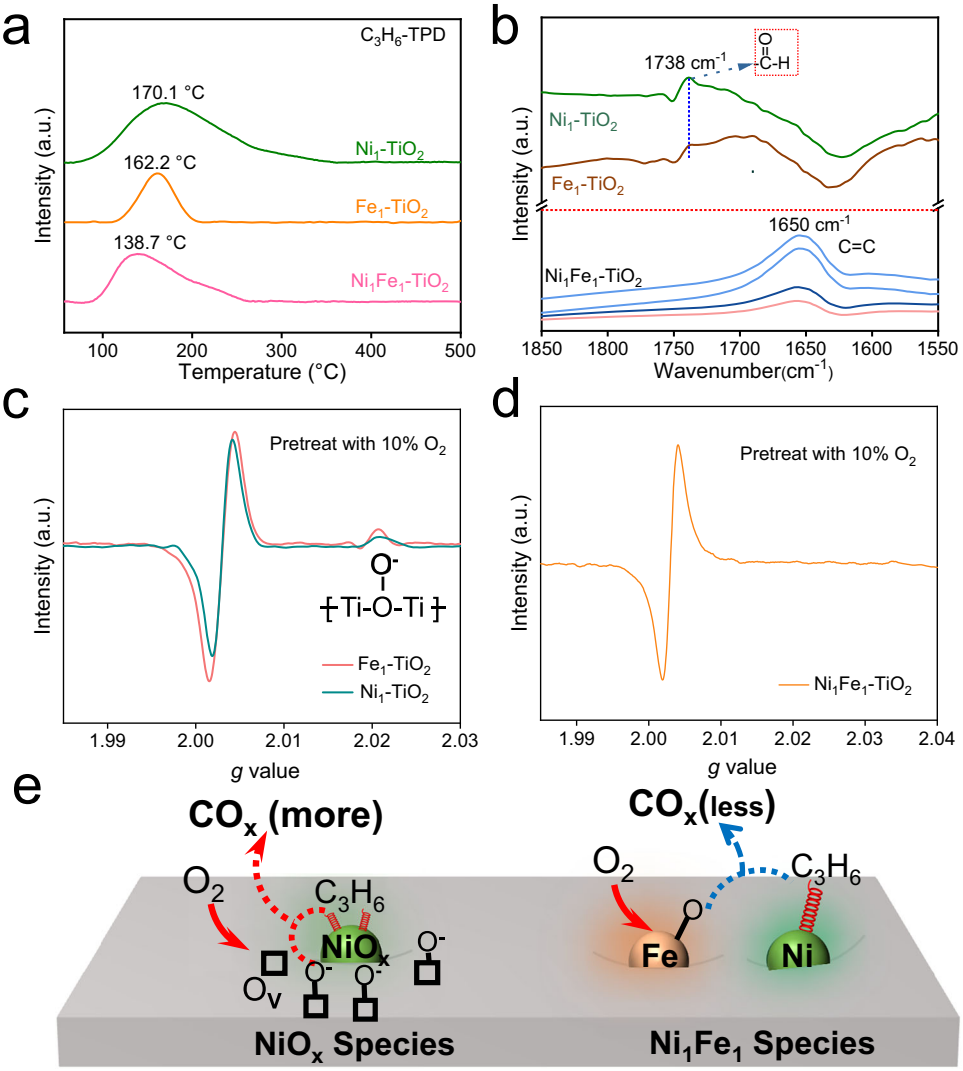

Fig. 5 | Mechanism of CO_x inhibition. a C_3H_6-TPD analysis of of Ni_1-TiO_2, Fe_1-TiO_2 and Ni_1Fe_1-TiO_2. **b** In-situ FT-IR spectra of Ni_1Fe_1-TiO_2 with 10 vol% C_3H_8/Ar (10 mL/min) and 10 vol% O_2/Ar (10 mL/min), (350–500 °C, recorded at intervals of 50 °C, down to top), Fe_1-TiO_2 (500 °C) and Ni_1-TiO_2 (500 °C) at enlarge view 1850–1550 cm^{-1}. **c**, **d** EPR spectra of Ni_1-TiO_2, Fe_1-TiO_2, and Ni_1Fe_1-TiO_2 after pretreatment with 10% O_2/Ar. **e** Schematic diagram of CO_x formation.

and anatase TiO_2 (see below for molar ratios) were ground (grinding should be performed at ≤40% relative humidity to prevent K_2CO_3 deliquescence.) and calcined at 1000 °C for 1 h, followed by regrinding and calcination at 1000 °C for 20 h. The molar ratios of the reactants were determined according to the following equations:

$$\text{For } M^{2+}\text{ (MnO, CoO, NiO): } K_{0.8}Ti_{(5.2-x)/3}Li_{(0.8-2x)/3}M_xO_4 \quad (1)$$

$$\text{For } M^{3+}\text{ (Fe_2O_3): } K_{0.8}Ti_{(5.2-2x)/3}Li_{(0.8-x)/3}M_xO_4 \quad (2)$$

With Ni_1-TiO_2 as an example, the doping ratio of Ni is $x = 0.2$. According to formula 1, we can calculate the molar ratios of different components ($K_{0.8}Ti_{1.67}Li_{0.13}Ni_{0.2}O_4$). K_2CO_3 (0.04 mol (K^+ = 0.08 mol), 5.53 g), rutile TiO_2 (0.167 mol, 13.3 g), NiO (0.02 mol, 1.5 g) and Li_2CO_3 (0.0065 mol (Li^+ = 0.013 mol), 0.48 g) were ground for 1 h and calcined at 900 °C for 1.5 h. The product after calcination was ground again for 1 h and calcined at 1000 °C for 20 h to yield layered titanate. The titanate was then protonated by treatment with 1 mol L^{-1} HCl (100 mL/g titanate) with daily replacement of the HCl solution for 3 days. Acid washing with hydrochloric acid exchanges interlayer K^+ and Li^+ for protons and removes surface undoped metals, as reported in previous literature. The resulting catalysis was washed with distilled water until neutral and dried under vacuum.

$M_1M'_1$-TiO_2 nanosheets. $M_1M'_1$-TiO_2 nanosheets ($M_1M'_1$ = Ni_1Fe_1, Ni_1Co_1, Ni_1Mn_1, Fe_1Co_1, Fe_1Mn_1, Co_1Mn_1) were synthesized following the procedure for M_1-TiO_2 nanosheets, using the general formula $K_{0.8}Ti_{(5.2-3(x+y))/3}Li_{0.8/3}M_xN_yO_4$ to determine the molar ratios of the metal oxides. With Ni_1Fe_1-TiO_2 as an example, the doping ratio is $x = 0.1$ for Ni and $y = 0.1$ for Fe. According to the formula, we can calculate the molar ratios of different components ($K_{0.8}Ti_{1.53}Li_{0.26}Ni_{0.1}Fe_{0.1}O_4$). K_2CO_3 (0.04 mol (K^+ = 0.08 mol), 5.53 g), rutile TiO_2 (0.153 mol, 12.22 g), NiO (0.01 mol, 0.75 g), Fe_2O_3 (0.005 mol (Fe^{3+} = 0.01 mol), 0.8 g) and Li_2CO_3 (0.013 mol (Li^+ = 0.026 mol), 0.96 g) were ground for 1 h and calcined at 900 °C for 1.5 h. The product after calcination was ground again for 1 h and calcined at 1000 °C for 20 h to yield layered titanate. The subsequent processing method is consistent with the preparation method of the M1-TiO_2 catalyst.

Catalyst shaping process. A catalyst precursor was prepared by ball-milling 250 g of catalyst powder with 50 g of hydroxypropyl cellulose

(HPC) binder in a jar mill for 10 h at 300 rpm. Water was added to the powder mixture in a kneader to achieve a water-to-powder mass ratio of 0.1. The water was introduced gradually over 10 min to ensure uniform distribution. Kneading was then continued to achieve a homogeneous paste. The resulting paste was extruded through a twin-screw extruder at a screw speed of 7–10 rpm to produce catalyst strips. The extruded strips were dried in an oven and subsequently calcined in a muffle furnace to obtain the final clover-shaped catalyst.

Material characterizations

The physicochemical properties of the catalysts were characterized using a variety of techniques.

X-ray diffraction (XRD). Crystalline phases were identified by powder X-ray diffraction using a Rigaku D/Max-2500 diffractometer equipped with a Shimadzu detector and Cu Kα radiation ($\lambda = 1.5418$ Å). The operating conditions were 100 mA and 40 kV, with a scan range of 10–90° 2θ and a scan rate of 5.0°/min.

Transmission electron microscopy (TEM). The morphology and microstructure of the catalysts were investigated using a JEOL 2100 F transmission electron microscope operating at an accelerating voltage of 200 kV. High-angle annular dark-field scanning transmission electron microscopy (HAADF-STEM) images were acquired on a JEM-ARM300F microscope.

X-ray photoelectron spectroscopy (XPS). Surface elemental composition and chemical states were analyzed by X-ray photoelectron spectroscopy (XPS) using an ESCALAB250XI spectrometer (Thermo Fisher Scientific).

X-ray absorption near-edge structure (XANES). XANES measurements at the K-edge were performed at beamline 1W1B at the Beijing Synchrotron Radiation Facility (BSRF) in total electron yield (TEY) mode. The electron energy was 2.5 GeV with a beam current of 250 mA. Data processing, including energy calibration, background subtraction, and normalization, was carried out using the Athena software package. Extended X-ray absorption fine structure (EXAFS) analysis was performed using the Artemis module of IFEFFIT. The χ (k) data were Fourier transformed to R-space using a Hanning window ($d_k = 1.0$ Å^{-1}) over a k-range of 2–12 Å^{-1}. Least-squares curve fitting was performed in R-space to obtain quantitative structural information.

Temperature-programmed desorption (TPD). TPD of O_2, C_3H_8, and C_3H_6 was performed using an AutoChemII 2920 chemisorption analyzer. Before each experiment, the sample was pretreated by heating to 300 °C at a rate of 10 °C/min under a He flow (30 mL/min) and held for 1 h to remove any adsorbed species. After cooling to 50 °C, the sample was exposed to a 10% O_2/He mixture (30 mL/min) for 2 h for O_2-TPD, or to pure C_3H_8 or C_3H_6 (30 mL/min) for 2 h for hydrocarbon TPD. Weakly adsorbed species were removed by purging with He (30 mL/min) for 1 h. Finally, the temperature was ramped to 800 °C at a rate of 10 °C/min under He flow, and the desorbed species were monitored using a thermal conductivity detector (TCD).

In-situ diffuse reflectance infrared Fourier transform spectroscopy (DRIFTS). In-situ DRIFTS measurements were conducted using a Bruker Tensor II spectrometer equipped with a mercury cadmium telluride (MCT) detector and CaF_2 windows. Spectra were acquired in the range of 900–3800 cm^{-1} with a resolution of 4 cm^{-1} and an accumulation of 32 scans. A 100 mg sample of catalyst was loaded into the in-situ reaction cell and pretreated in pure Ar at 250 °C for 1 h (flow rate: 10 mL/min) to remove adsorbed species. After cooling to 50 °C, a background spectrum was collected under Ar flow. A reaction gas mixture of 10 vol% C_3H_8/Ar (10 mL/min) and 10 vol% O_2/Ar (10 mL/min) was then introduced into the cell, and spectra were recorded. The cell was subsequently heated to the desired temperature over 30 min, and further spectra were acquired.

C_3H_6-desorption FT-IR experiments were performed using the same spectrometer. The catalyst was pretreated in pure Ar at 250 °C for 1 h (flow rate: 10 mL/min) and then cooled to room temperature. A background spectrum was collected. C_3H_6/Ar (10 vol% C_3H_6) was introduced into the cell at a flow rate of 10 mL/min for 1 h to ensure saturated adsorption of C_3H_6 on the catalyst surface. The gas flow was then switched to pure Ar (5 mL/min) to initiate the desorption process. IR spectra were recorded at 2 min intervals. Desorbed species were analyzed using a downstream quadrupole mass spectrometer, and the characteristic peaks for water ($m/z = 18$) and argon ($m/z = 20$) were integrated to quantify desorption products.

In-situ XANES measurements. In-situ X-ray absorption near-edge structure (XANES) measurements at the Ni and Fe K-edges were performed in transmission mode at beamline 1W1B of the Beijing Synchrotron Radiation Facility (BSRF). The catalyst sample was pressed into a self-supporting wafer and loaded into a reaction microdevice equipped with Be windows. The sample was heated to 200 °C under a high-purity He flow and held for 30 min. A reaction gas mixture of C_3H_8/He 10 vol% (10 mL/min) and 10 vol% O_2/Ar (10 mL/min) was then introduced into the cell, and XANES spectra were collected. The cell was subsequently heated to the desired temperature over 30 min, and further XANES spectra were acquired. All XANES data were processed using the Athena software package.

In-situ XANES measurements at different atmospheres. The catalyst sample was heated to 520 °C under a high-purity He flow and held for 30 min before acquiring XANES spectra. A gas mixture of C_3H_8 (10 mL/min) was then introduced into the cell, and spectra were collected after 1 h. O_2 (10 mL/min) was then added to the gas flow, and XANES spectra were acquired at 1 h intervals. Finally, the C_3H_8 flow was stopped, and after 30 min, the final XANES spectra were collected.

In-situ X-ray emission spectroscopy (XES) measurements at different atmospheres. In-situ XES measurements were performed using a von Hamos-geometry wavelength-dispersive X-ray spectrometer at the BL14W1-XANES beamline of the Shanghai Synchrotron Radiation Facility (SSRF). Ni $K\beta_{2,5}$ and Fe $K\beta_{2,5}$ emission lines were collected using Si (551) and Si (531) cylindrically bent crystal analyzers, respectively, with a radius of curvature of 25 cm. A Pilatus 100 K detector equipped with CMOS sensors was used to collect the dispersed fluorescence. Kohzu positioning stages were used for the precise alignment of the spectrometer components. The electron storage ring operated at 3.5 GeV with a beam current of 240 mA in top-up injection mode. The photon flux of the BL14W1-XANES beamline was 5×10^{12} phs s^{-1} at 10 keV, with a Si (111) double-crystal monochromator and a beam size of 100 × 200 μm^2 (vertical × horizontal).

The catalyst sample was heated to 520 °C under a high-purity He flow and held for 30 min before acquiring XES spectra. A gas mixture of C_3H_8 (10 mL/min) and N_2 (10 mL/min) was then introduced into the cell, and spectra were collected after 1 h. O_2 (10 mL/min) was then added to the gas flow, and XES spectra were acquired at 1 h intervals. Finally, the C_3H_8 flow was stopped, and after 30 min, the final XES spectra were collected.

$^{18}O_2$ isotopic tracer studies. Isotopic tracer studies were conducted using $^{18}O_2$ in a high-temperature reaction chamber. A 100 mg sample of catalyst was placed in the cell and pretreated in 10% $^{16}O_2$/90% He at 773 K for 1 h. After purging with pure He for 10 min, the gas flow was switched to a mixture of 10% $^{18}O_2$/He and 10% C_3H_8/He at a flow rate of

5 mL/min. The isotopic composition of the reactor effluent was monitored using an online mass spectrometer (Shimadzu QP2010Plus) at 6 s intervals.

Catalytic performance evaluation

The catalytic performance for oxidative dehydrogenation of propane (ODHP) was evaluated in a fixed-bed reactor (Torch Instrument Co., LTD) using a quartz tube reactor (outer diameter: 8 mm, inner diameter: 6 mm, length: 480 mm) at a pressure of 0.1 MPa. Mass flow controllers (BROOKS Instruments Co., Ltd.) were used to regulate the flow of feed gases. The catalyst was initially received in tablet form. The catalyst was sieved to 60 mesh and 150 mg was loaded into the reactor, positioning it within the isothermal zone of the furnace The reaction temperature was controlled using two thermocouples, one placed in the furnace and the other in the quartz tube near the catalyst bed, with a heating rate of 10 °C/min. The feed gas consisted of a $C_3H_8/O_2/N_2$ mixture with a volume ratio of 1:1:1, and the weight hourly space velocity (WHSV) was maintained at 8.8 h^{-1}. The total gas flow used in the experiments was $C_3H_8{:}O_2{:}N_2 = 12{:}12{:}12$ (mL/min). The catalyst was tested without any pretreatment. The composition of the reactor effluent was analyzed online using a gas chromatograph (PANNA A91) equipped with a flame ionization detector (FID) and a thermal conductivity detector (TCD). A capillary column (Agilent, HP-AL/S, 25 m * 0.32 mm * 8 μm) with FID for hydrocarbons and TCD for inorganic gases (H_2, N_2, O_2, CH_4, CO, CO_2) was used for chromatographic analysis. The TCD detector utilized a multi-column system consisting of 1-meter and 2 meter HaySep columns followed by a 3 meter 5 A molecular sieve column for the separation of H_2, CO_2, O_2, N_2, CH_4, and CO. Propane conversion and product selectivity were calculated based on the corrected peak area normalization method.

Data Analysis

Propane and oxygen conversion were calculated using the following Eqs. (3–4):

$$C_3H_8 \text{ conversion: } X_{C_3H_8}(\%) = \frac{\left[F_{C_3H_8}\right]_{in} - \left[F_{C_3H_8}\right]_{out}}{\left[F_{C_3H_8}\right]_{in}} \times 100 \quad (3)$$

$$O_2 \text{ conversion: } X_{O_2}(\%) = \frac{\left[F_{O_2}\right]_{in} - \left[F_{O_2}\right]_{out}}{\left[F_{O_2}\right]_{in}} \times 100 \quad (4)$$

where, $F^{in}_{C_3H_8}$ and $F^{out}_{C_3H_8}$ indicate the inlet and outlet flow rates of x (mL·min^{-1}), respectively.

Selectivity of hydrocarbon products is calculated as follows:

$$\text{Sel}(\%) = \frac{n_i \times [F_i]_{out}}{\left(\sum n_i \times [F_i]_{out}\right)} \times 100 \quad (5)$$

Where i represents the hydrocarbon products in the effluent gas, ni is the number of carbon atoms of the component i, and Fi is the corresponding flow rate.

The carbon balance of products was determined from below:

$$\text{C balance} = \frac{\left(\sum n_i \times [F_i]_{out} + 3 \times \left[F_{C_3H_8}\right]_{out}\right)}{3 \times \left[F_{C_3H_8}\right]_{in}} \times 100 \quad (6)$$

Computational details

All theoretical calculations were performed using the Vienna Ab-Initio Simulation Package (VASP, version 5.4.4) based on the plane-wave pseudopotential density functional theory (DFT) methods. The projector-augmented wave (PAW) method was used to describe the electron-core interaction. The kinetic cut-off energy of the plane-wave basis set was 400 eV, and single gamma-point sampling was used for Brillouin zone integration. The total energy and forces convergence thresholds for the geometry optimization were set to 10−5 eV and 0.02 eV Å^{-1}, respectively. The vacuum spacing of 18 Å was added to Ni_1Fe_1-TiO_2 to avoid interactions between the layer plane along the z-direction in our manuscript. The TiO_2 surface was modeled for all DFT calculations, we finally used a hexagonal unit cell with a = 15.012 Å, b = 15.012 Å, and c = 18.342 Å.

Data availability

All data generated during this study are included in this article and its Supplementary Information. Source data are provided with this paper.

References

1. Chen, S. et al. Defective TiO_x overlayers catalyze propane dehydrogenation promoted by base metals. *Science* **385**, 295–300 (2024).
2. Sun, G. et al. Metastable gallium hydride-mediated propane dehydrogenation with H2 cofeeding. *Nat. Chem.* **16**, 575–583 (2024).
3. Tabanelli, T. et al. A career in catalysis: fabrizio cavani. *ACS Catal.* **13**, 14131–14154 (2023).
4. Yan, H. et al. Tandem In_2O_3-Pt/Al_2O_3 catalyst for coupling of propane dehydrogenation to selective H_2 combustion. *Science* **371**, 1257–1260 (2021).
5. Zhou, H. et al. Isolated boron in zeolite for oxidative dehydrogenation of propane. *Science* **372**, 76–80 (2021).
6. Wang, W. et al. Tandem propane dehydrogenation and surface oxidation catalysts for selective propylene synthesis. *Science* **381**, 886–890 (2023).
7. Almallahi, R., Wortman, J. & Linic, S. Overcoming limitations in propane dehydrogenation by codesigning catalyst-membrane systems. *Science* **383**, 1325–1331 (2024).
8. Mitran, G. et al. Propane oxidative dehydrogenation over VO_x/SBA–15 catalysts. *Catal. Today* **306**, 260–267 (2018).
9. Abello, M., Gomez, M. & Ferretti, O. Mo/γ-Al_2O_3 catalysts for the oxidative dehydrogenation of propane: effect of Mo loading. *Appl. Catal. A Gen.* **207**, 421–431 (2001).
10. Abello, M. C., Gomez, M. F. & Ferretti, O. NbO_x/CeO_2-rods catalysts for oxidative dehydrogenation of propane: Nb–CeO_2 interaction and reaction mechanism. *J. Catal.* **348**, 189–199 (2017).
11. Li, H. et al. Dehydrogenation of ethylbenzene and propane over Ga_2O_3–ZrO_2 catalysts in the presence of CO_2. *Catal. Commun.* **8**, 1317–1322 (2007).
12. Monguen, C. K. F. et al. Oxidative dehydrogenation of propane into propene over chromium oxides. *Ind. Eng. Chem. Res.* **61**, 4546–4560 (2022).
13. Li, X. et al. How to control selectivity in alkane oxidation? *Chem. Sci.* **10**, 2429–2443 (2019).
14. Grant, J. T., Venegas, J. M., McDermott, W. P. & Hermans, I. Aerobic oxidations of light alkanes over solid metal oxide catalysts. *Chem. Rev.* **118**, 2769–2815 (2018).
15. Hannagan, R. T., Giannakakis, G., Flytzani-Stephanopoulos, M. & Sykes, E. C. H. Single-atom alloy catalysis. *Chem. Rev.* **120**, 12044–12088 (2020).
16. Campos, J. Bimetallic cooperation across the periodic table. *Nat. Rev. Chem.* **4**, 696–702 (2020).
17. Zhang, J. et al. Importance of species heterogeneity in supported metal catalysts. *J. Am. Chem. Soc.* **12**, 5108–5115 (2022).
18. Ro, I. et al. Bifunctional hydroformylation on heterogeneous Rh-WO_x pair site catalysts. *Nature* **609**, 287–292 (2022).
19. Cheng, K. et al. Maximizing noble metal utilization in solid catalysts by control of nanoparticle location. *Science* **377**, 204–208 (2022).

20. Hai, X. et al. Geminal-atom catalysis for cross-coupling. *Nature* **622**, 754–760 (2023).
21. Liang, Y., Zhang, X. & MacMillan, D. W. C. Decarboxylative sp^3 C–N coupling via dual copper and photoredox catalysis. *Nature* **559**, 83–88 (2018).
22. Lu, F. et al. Engineering platinum–oxygen dual catalytic sites via charge transfer towards highly efficient hydrogen evolution. *Angew. Chem. Int. Ed.* **59**, 17712–17718 (2020).
23. Yi, D. et al. Regulating charge transfer of lattice oxygen in single-atom-doped titania for hydrogen evolution. *Angew. Chem. Int. Ed.* **59**, 15855–15859 (2020).
24. Pan, L. et al. Single-atom or dual-atom in TiO_2 nanosheet: which is the better choice for electrocatalytic urea synthesis? *Angew. Chem. Int. Ed* **62**, e202216835 (2023).
25. Zhao, Y. et al. Optimized NiFe-based coordination polymer catalysts: sulfur-tuning and operando monitoring of water oxidation. *ACS Nano* **16**, 15318–15327 (2022).
26. Yang, Y. et al. Perspectives on multifunctional catalysts derived from layered double hydroxides toward upgrading reactions of biomass resources. *ACS Catal.* **11**, 6440–6454 (2021).
27. Liu, W. et al. Atomically-ordered active sites in NiMo intermetallic compound toward low-pressure hydrodeoxygenation of furfural. *Appl. Catal. B. Environ.* **282**, 119569 (2021).
28. Caserta, G. et al. Stepwise assembly of the active site of [NiFe]-hydrogenase. *Nat. Chem. Biol.* **19**, 498–506 (2023).
29. Jiang, H. et al. Bio-derived hierarchical multicore–shell Fe_2N-nanoparticle-impregnated N-doped carbon nanofiber bundles: a host material for lithium-/potassium-ion storage *Nano. Micro Lett.* **11**, 1–17 (2019).
30. Zitolo, A. et al. Identification of catalytic sites for oxygen reduction in iron-and nitrogen-doped graphene materials. *Nat. Mater.* **14**, 937–942 (2015).
31. Osada, M. et al. Controlled doping of semiconducting titania nanosheets for tailored spinelectronic materials. *Nanoscale* **6**, 14227–14236 (2014).
32. Safeer, M. et al. Remarkable CO_x tolerance of Ni^{3+} active species in a Ni_2O_3 catalyst for sustained electrochemical urea oxidation. *J. Mater. Chem. A.* **10**, 4209–4221 (2022).
33. Wu, H. et al. Control on the formation of Fe_3O_4 nanoparticles on chemically reduced graphene oxide surfaces. *CrystEngComm* **14**, 499–504 (2012).
34. Gambo, Y. et al. Catalyst design and tuning for oxidative dehydrogenation of propane–a review. *Appl. Catal A. Gen.* **609**, 117914 (2021).
35. Smolentsev, G. et al. X-ray emission spectroscopy to study ligand valence orbitals in Mn coordination complexes. *J. Am. Chem. Soc.* **131**, 13161–13167 (2009).
36. Hugenbruch, S. et al. In search of metal hydrides: an X-ray absorption and emission study of [NiFe] hydrogenase model complexes. *Phys. Chem. Chem. Phys.* **18**, 10688–10699 (2016).
37. Pollock, C. J. et al. Experimentally quantifying small-molecule bond activation using valence-to-core X-ray emission spectroscopy. *J. Am. Chem. Soc.* **135**, 11803–11808 (2013).
38. Pantazidisa, A. et al. A TAP reactor investigation of the oxidative dehydrogenation of propane over a V–Mg–O catalyst. *Catal. Today* **40**, 207–214 (1998).
39. Chen, K., Bell, A. T. & Iglesia, E. Kinetics and mechanism of oxidative dehydrogenation of propane on vanadium, molybdenum and tungsten oxides. *J. Phys. Chem. B.* **104**, 1292–1299 (2000).
40. Lin, M. et al. Selective oxidation of propane to acrylic acid with molecular oxygen. *Appl. Catal. A* **207**, 1–16 (2001).
41. Lin, M. et al. Reaction pathways in the selective oxidation of propane over a mixed metal oxide catalyst. *Catal. Today.* **61**, 223–229 (2000).
42. Shi, S. C. et al. Preparation of aldehyde-graphene quantum dots from glucose for controlled release of anticancer drug. *Front. Mater.* **10**, 1180745 (2023).
43. Fan, Q. G. et al. Characterization of cellulose aldehyde using fourier transform infrared spectroscopy. *J. Appl. Polym. Sci.* **82**, 1195–1202 (2001).
44. Priebe, J. B. et al. Water reduction with visible light: synergy between optical transitions and electron transfer in Au-TiO2 catalysts visualized by in-situ EPR spectroscopy. *Angew. Chem. Int. Ed.* **52**, 11420–11424 (2013).
45. Howe, R. F. & Gratzel, M. EPR study of hydrated anatase under UV irradiation. *J. Phys. Chem.* **91**, 3906–3909 (1987).

Acknowledgements

This work was supported by the Fundamental Research Funds for the Central Universities (2024JBZY007) and the Guangdong S&T Program (No. 2020B0101370001). We thank the beamlines BL14W1 and BL11B at Shanghai Synchrotron Radiation Facility (SSRF), beamlines 1W1B at Beijing Synchrotron Radiation Facility (BSRF), and the Beamlines MCD-A and MCD-B (Soochow Beamline for Energy Materials) at National Synchrotron Radiation Laboratory (NSRL), and Anhui Absorption Spectroscopy Analysis Instrument Co, Ltd. for XAFS measurements and analysis. We thank the staff members at BL01B beamline of the National Facility for Protein Science in Shanghai (NFPS), Shanghai Advanced Research Institute, Chinese Academy of Sciences, for providing technical support and assistance in data collection and analysis. The work carried out at Brookhaven National Laboratory was supported by the US Department of Energy, Office of Science, Office of Basic Energy Sciences, Chemical Sciences, Geosciences, and Biosciences (GSGB) Division, Catalysis Science Program under contract No. DE-SC0012704.

Author contributions

Y.Y. and J.W. conceptualized the project under the supervision of S.D.S. and X.W.; Y.Y. synthesized catalysts, performed the performance tests, and analyzed experimental data with the help of F.L., W.L., F.Y. and G.J.; J.W. performed DFT simulation; L.Z. conducted the TEM characterization; B.M. carried out in situ XES and XANFS measurements and analyses with the assistance of W.Y.; Y.Y. wrote the paper. All authors discussed the results and commented on the paper.

Competing interests

The authors declare no competing interests.

Additional information

Supplementary information The online version contains supplementary material available at https://doi.org/10.1038/s41467-025-59376-z.

Correspondence and requests for materials should be addressed to Sanjaya D. Senanayake or Xi Wang.

Peer review information *Nature Communications* thanks the anonymous reviewers for their contribution to the peer review of this work. A peer review file is available.